Reverse Micelle Mediated synthesis of Calcium Phosphate Nanocarriers for Controlled Release of Bovine Serum Albumin (BSA)

Sudip Dasgupta, **Amit Bandyopadhyay**, and **Susmita Bose**
W. M. Keck Biomedical Materials Research Laboratory, School of Mechanical and Materials Engineering, Washington State University, Pullman, WA 99164

Abstract

Calcium phosphate (CaP) nanoparticle with calcium to phosphorus (Ca:P) molar ratio of 1.5:1 were synthesized using reverse micro emulsion. $Ca(NO_3)_2.4H_2O$ and H_3PO_4 were used as aqueous phase, cyclohexane as organic phase, and poly(oxyethylene)$_{12}$ nonylphenol ether (NP-12) as surfactant. Depending on calcination temperature between 600 and 800 °C, CaP nanoparticle showed different phases calcium deficient hydroxyapatite (CDHA) and β-tricalcium phosphate (β-TCP), particle size between 48 and 69 nm, the BET specific average surface area between 73 m^2/g and 57 m^2/g. Bovine serum albumin (BSA) was used as a model protein to study loading and release behavior. Adsorptive property of BSA was investigated with the change in BET surface area of these nanoparticle and the pH of the suspension. At pH 7.5, maximum amount of BSA was adsorbed onto CaP nanoparticle. The release kinetics of BSA showed a gradual time dependent increase at pH 4.0 and 6.0 buffer solutions. However, the amount of released protein was significantly smaller at pH 7.2. BSA release rate also varied depending on the presence of different phases of CaPs in the system, β-TCP or CDHA. These results suggest that BSA protein release rate can be controlled by changing particle size, surface area and phase composition of CaP nanocarriers.

Keywords

Tricalcium phosphate (TCP); Calcium deficient hydroxyapatite (CDHA); Phase; Reverse micelle; Protein; Controlled release

1. Introduction

The prospect of cellular delivery involving transfer of various drugs and bio-active molecules, such as peptides, proteins and DNAs, through the cell membrane into cells has opened up many promises in the fields of medicine and drug delivery. The direct delivery of drugs and biomolecules is generally inefficient because of their low bioavailability, susceptibility to enzymatic degradation and detrimental side effects.[1,2] Delivery of drugs and biomolecules at nanoscale into body makes them much more bioavailable, soluble, and safe.[3] In addition to enhanced solubility, the improved performance of drugs and biomolecules in nanoparticulate form is attributed to its compatibility with nanosized receptors present on the cell surface.

Nanocarriers can reduce the possibility of enzymatic degradation and hazardous side effects of drugs and biomolecules carried by it.[1–3]

Inorganic nanoparticles as new non-viral carriers have immense potential as drug and biomolecule carrier system. Risk of immune response, a common problem with viral vectors, 4 is reduced with inorganic NP based carrier system. Most of the inorganic nanoparticles are non–toxic or mildly toxic to living cells.5 Unlike liposome, inorganic nanocarriers are resistant to degradation in contact with bile salts and lipases.[6] Above all, surface functionalization in inorganic nanoparticles is relatively easy which attributes to their potential capability of targeted delivery and controlled release of carried drugs and biomolecules. Many inorganic materials, such as calcium phosphate (CaP),[7] silicon oxide,8 gold,9−12 carbon materials, 13, 14 iron oxide,15,16 and layered double hydroxide (LDH),[17] have been studied as a carrier for biomolecules. Nano-CaPs are found to be one of the most promising among them primarily because of their excellent biocompatibility and biodegradability18−20 in physiological environment. Most commonly used synthetic CaPs in orthopedic and dentistry are bioactive hydroxyapatite (HA, $Ca_{10}(PO_4)_6(OH)_2$) and bioresorbable tricalcium phosphate (TCP, $Ca_3(PO_4)_2$).

HA has excellent affinity to biological substances, such as collagen, proteins, enzymes, cells, and viruses because of it's bioactivity.19,20 HA scaffold impregnated with growth factors has been investigated for bone regeneration.21,22 Ono et al. used HA granules with bone morphogenetic protein (BMP) and revealed new bone formation around HA granules.23 Liu et al. studied bovine serum albumin (BSA) loaded calcium deficient hydroxyapatite (CDHA) nanocarriers for drug delivery.24 The effect of powder crystallinity and surface area on loading and release of cytochrome-c from HA nanoparticles was investigated by Matsumoto et al.25 TCP being much more bioresorbable than HA, offers significant opportunities to be used as a carrier for controlled release of drugs and biomolecules. Cho et al. found recombinant human bone morphogenetic protein-4 (rhBMP-4) loaded β-TCP particles, with particle size between 50 and 500 µm, did not exert any particle size effect on bone formation in rat calvarial defects. 26 Recombinant human transforming growth factor-b 1 (rhTGF-b 1) carrying capability of collagen-HA/ TCP microspheres was investigated by Hsu et al.27 Active bone with mature marrow tissue formation was observed in the bone defect treated with Col-HA/TCP microspheres containing rhTGF-b1. Due to wide availability of BSA in human physiological system, BSA is an attractive model protein. In our recent work we have shown that mesoporous calcium silicate systems can be chemically synthesized where acid treatment produces different porosity to study controlled release of BSA over two weeks time period.28

To the best of our knowledge, use of TCP nanocarriers as controlled release system has not been reported in literature. Since bioresorbability of CaP based nanoparticles vary depending on their phase purity and composition, it is interesting to study how protein loading and release can be controlled from CDHA and β-TCP nanocarriers. Here we report synthesis of calcium phosphate nanoparticles (nano-CaPs) using reverse micelle based template system and study the possibility of using these nano-CaPs as a carrier for controlled release of BSA as model protein. BSA is a protein with well defined primary structure and high content of charged amino acids. Thus BSA can be easily adsorbed on CaP NP surface by electrostatic interaction. Depending on the calcination temperature, phase pure CDHA and β-TCP nanoparticles can be obtained. The variation in BSA adsorption is evaluated with change in particle size, surface area, phase composition, and pH of BSA-nanoparticle suspension to examine if BSA release can be controlled. Release behavior of resulting BSA-loaded nano-CaPs is presented and compared with the dissolution kinetics of nano-CaPs under the same experimental conditions.

2. Materials and Methods

2.1 Synthesis of CaP nanoparticles

Nano-CaPs were synthesized using a similar reverse micelle based method established in our laboratory which was used to synthesize hydroxyapatite nanoparticle.[29–31] In the present system Ca to P molar ratio in the precursor chemical was kept at 1.5:1 to synthesize tricalcium phosphate. 5M aqueous solution of Ca^{2+}-ion was prepared by dissolving 0.03 moles of calcium nitrate tetrahydrate $[Ca(NO_3)_2, 4H_2O$, J. T. Baker, Phillipsburg, NJ] in 6 ml distilled water. 0.02 moles of 85.7 wt% orthophosphoric acid (H_3PO_4, Fisher Scientific, Fair Lawn, NJ) was added to the system to maintain Ca to P molar ratio 1.5:1. Ninety ml of cyclohexane (J. T. Baker, Phillipsburg, NJ) was added to the aqueous phase to maintain aqueous to organic phase ratio (aq:org) of 1:15 in the mixture. Ten volume% of poly (oxyethylene)$_{12}$ nonylphenol ether (NP 12, Sigma-Aldrich, St. Louis, MO) was added as surafctant to the mixture with vigorous stirring to prepare water-in-oil emulsion. The pH of the medium was adjusted to 9 with drop-wise addition of ammonium hydroxide (NH_4OH, J. T. baker, Phillipsburg, NJ) and then the reaction mixture was aged for 24h at room temperature. After aging, the emulsion was evaporated on the hot plate at 150 °C followed by complete drying at 450 °C. To remove the organic binders completely, we have reported previously that dried powders needed to be calcined at least at 600 °C.[29] Therefore, dried powder was calcined at 600, 700 and 800 °C for 4h to completely burn out organic residues and obtain high purity nanocrystalline CaP powder.

2.2 Physico-chemical properties of CaP nanoparticles

The phases of synthesized nano-CaPs calcined at 600, 700 and 800 °C were determined using a Philips fully automated x-ray diffractometer with Cu-K$_{\alpha}$ radiation (1.54018 A) and a Ni-filter operated at 35 kV and 30 mA. Dynamic light scattering technique (NICOMP™ 380, Santa Barbara, CA, USA) was used to determine particle size distribution of nano-CaPs. Morphology of nano-CaPs was studied using a transmission electron microscope (TEM, JEOL, JEM 120 MA, USA) set at an accelerating voltage of 100 kV. The aspect ratio of nano-CaPs was calculated from TEM images using soft imaging system, analysis 3.2 (Lakewood, CO, USA). Specific average surface area of nano-CaPs was determined by Brunauer, Emmett and Teller (BET) method (5 points analyzer, Tristar Micromeritics, USA) with a continuous flow of nitrogen. Three samples from each powder were used for the BET surface area measurement and data were presented as mean ± standard deviation. Fourier transform infrared (FTIR) spectra of nano-CaPs were obtained using an ATR- FTIR spectrophotometer (Nicolet 6700 FTIR, Madison, WI, USA) in the 400–4000 cm^{-1} wave number range.

2.3 BSA loading on CaP nanoparticles

Stock suspension of nano-CaPs (10 mg/ml) in water was prepared. Separately, BSA (Sigma-Aldrich, St. Louis, MO) stock solution (5 mg/ml) in water was prepared and diluted in water to various concentrations of BSA (0.5, 1.5, 2.5, 3.5, 5 mg/ml). 1 ml of each of the above BSA solutions was mixed with 4 ml of nanoparticles suspension in phosphate buffer solution at pH 7.5 on a shaker for 6 h at 37 °C. Then samples were centrifuged at 8000 rpm, washed with water and the supernatants were analyzed for the BSA concentration using UV spectrophotometer at 570 nm for comparison to establish standard curves. The amount of BSA adsorption per unit mass of nano-CaPs were then determined using the equation $(BSA)_{adsorbed} = ([BSA]_o - [BSA]_s)/W_{CaP}$, where $[BSA]_o$ represented total amount (μg) of BSA initially present in the suspension, $[BSA]_s$ represented total amount (μg) of BSA present in the supernatant, and W_{CaP} represented the total amount (mg) of nano-CaPs present in the suspension. After washing with distilled water, the BSA adsorbed nano-CaPs were dried at room temperature and stored at −10 °C in a freezer.

Background-corrected FTIR spectra of BSA loaded nano-CaPs were analyzed in the amide I band regions for their component compositions and peak frequencies. Gaussian curve-fitting, using GRAMS/386, was performed on the original (non-smoothed) amide I band region. The number of components and their peak positions were used as starting parameters. In all cases, linear baseline was fitted. The secondary structure content was calculated from the areas of the individually assigned bands and their fraction of the total area in the amide I region.[32] Calculated areas were averaged, and standard deviations were calculated.

2.4 Study of release kinetics of BSA from CaP nanoparticles

Twenty mg of BSA loaded nano-CaPs were suspended in 20 ml buffer solution in three separate vials containing phosphate buffer solution (PBS) at pH 7.2±0.2, bis-tris HCl buffer solution at pH 6.1±0.1 and acetate buffer solution at pH 4.1±0.1. Sample vials were incubated at 37 °C with continuous shaking. In this study, we selected pH 4.1 solution on the assumption that the local pH around the ruffled border of osteoclasts varies between 4.0 and 5.0 during the bone remodeling period.[33,34] At early stage of inflammation the pH of blood remains around 5.0 to 6.0 which justifies the selection of pH 6.1, while PBS solution of pH 7.2 was chosen because of its resemblance to the pH of homeostatic body fluid. The vials were centrifuged and 0.5 ml of supernatants were removed at each time point, kept in cryovials and frozen at −10 °C. The sample vials were vortexed to resuspend the BSA-nano-CaPs, and placed back in the incubator. The released amount of BSA in the supernatant was measured by BCA protein assay at 0.5, 1, 2, 4, 6, 12 and 24 hours of time period. The rate of dissolution of nano-CaPs calcined at 600, 700 and 800 °C was evaluated by measuring Ca^{2+} ion concentration in buffer solution at different pH using atomic absorption spectrophotometer (AAS). Twenty mg of nano-CaPs calcined at different temperature was suspended separately in 10ml of pH 4.0, 6.0 and 7.2 buffer solutions. The suspension was centrifuged at different time interval and the supernatant was analyzed for Ca^{2+} ion concentration by AAS. The blank solution was prepared by adding 90.0 ml double distilled deionized water to 10.0 ml aqueous solution containing 1% NaCl, 20% HNO_3. Samples were prepared by combining 2.0 ml of sample from dissolution media to 0.2 ml aqueous solution containing 1% NaCl and 20% HNO_3. The samples were measured at 422.7 nm using a Vapan FS 220 (Mulgrave, Victoria, Australia) AAS with a VWR (San Diego, CA, USA) calcium lamp with a slit of 0.5 and a current of 10 mA.

2.5 Statistical Analysis

Statistical analysis of data was performed using the software package SAS 9.1 (Cary, NC, USA).[35] All quantitative tests were carried out in triplicate and then mean values with standard deviations were calculated. After verifying normal distribution and homogeneity of variance, one way analyses of variance (ANOVA) was done for comparison between groups at a significance level of $p < 0.05$. Finally, Tukey's test for pairwise multiple comparison was performed to detect significant differences between groups.

3. Results

3.1 Physical properties of synthesized nanoparticles

Figure 1 shows XRD pattern of nano-CaPs synthesized using ether based NP-12 surfactant after heat treatment at 600, 700 and 800 °C for 4 h. The nanoparticles calcined at 600 and 700 °C consisted of primarily CDHA phase (JCPDS No 09-0432), but β-TCP was the major phase (JCPDS No 09-0169) in CaP powder calcined at 800 °C, which is consistent with earlier reports. [36] The characteristic bands for the PO_4^{3-}, HPO_4^{2-} groups of synthesized nano-CaPs are shown in the FTIR plot, Figure 2. The number average particle size distribution data is shown in Figure 3, which illustrates that the mean particle diameter increased from 30 nm to 42 nm as the calcination temperature increased from 600 °C to 800 °C. TEM micrographs in Figure 4 revealed that with change in calcination temperature from 600 °C to 800 °C, the average aspect

ratio of powder particles decreased from 8.22 to 1.27. Figure 5 showed an expected decrease in average BET specific average surface area of CaP powders from 73 m^2/g to 57 m^2/g due to an increase in calcination temperature from 600 °C to 800 °C in which only statistically significant variation was observed between 600°C and 800°C surface area data where p= 0.0460.

3.2. BSA adsorption on CaP nanoparticles

The adsorbed amount of BSA on nanoparticle surface depended significantly on the pH of the suspension where BSA- NP interaction took place. The adsorption of BSA onto 600 °C calcined nano-CaPs was studied in suspensions at different pH of 7.5, 8.5, and 9. The maximum amount of BSA adsorption was observed at pH 7.5 and thereafter with increase in suspension pH, the amount of BSA adsorption onto particle surface decreased, as shown in Figure 6. The variation in BSA adsorption was statistically quite significant between pH 7.5 with both pH 8.5 and pH 9.0 (p < 0.001 in both cases), however, the variation was not statistically significant between pH 8.5 and pH 9.0. A schematic presentation of BSA – CaP interaction is shown in Figure 7. The adsorbed amount of BSA on nano-CaPs also changed depending on its average specific surface area as shown in Figure 8 though the difference was not statistically significant between 600, 700 and 800 °C calcined powders. Using various concentrations of BSA solutions, the results showed that the adsorbed amount of protein on nano-CaPs increased linearly first up to the range of 0–800 µg/ml of the protein solution, and then remained constant beyond 800 µg/ml. Powders calcined at 600 °C with average specific surface area of 73 m^2/g showed the highest amount of BSA adsorption of 89 µg/mg of TCP, whereas 78 µg/mg was adsorbed onto 800 °C calcined powders having an average specific surface area of 57 m^2/g. All adsorption of BSA protein was detected using FTIR analysis. The FTIR spectra of pure BSA and BSA loaded nano-CaPs are shown in Figure 9 for comparison.

3.3 Secondary structure analysis of BSA

The secondary structure of BSA adsorbed on CaP nanoparticles surface was analyzed using FTIR spectroscopy. Table 1 shows the compositional analysis of secondary structure in pure solid BSA powder and adsorbed BSA on CaP surface. The α-helix content as determined from FTIR spectra in amide –I region was found to be 30 %, 31% and 34% for 600, 700 and 800 °C calcined nano-CaPs, respectively. The result showed a decrease in α–helix content in CaP-BSA nanopowder as compared to α-helix content of 38% in pure solid BSA powder.

3.4 Release rate of protein from BSA adsorbed CaP nanoparticles

3.4.1 Effect of buffer pH on protein release rate—Figure 10a, b and c show the release rate of BSA from nano-CaPs immersed in pH 7.2, 6.1, and 4.1, respectively. For all nano-CaPs, the amount of released BSA gradually increased with time. However, for BSA adsorbed nanoparticles immersed in pH 7.2 solution, the amount of released protein was significantly smaller than that in pH 4.0 and pH 6.0 solutions as shown in Figure 10. Though the nanoparticles immersed in pH 4 and pH 6 exhibited almost 100% release of BSA within 24 hours of incubation, only 45 % of protein release was observed for Nano-CaPs immersed in pH 7.2 buffer within the same period of incubation time.

3.4.2 Effect of calcination temperature on protein release rate—Irrespective of pH of the buffer in which BSA-nano-CaPs were immersed, nanoparticles calcined at 800 °C always showed significantly higher (p < 0.0001 in all cases) protein release compared to nanoparticles calcined at 600 and 700 °C. The BSA release from 700 °C calcined particles was also significantly higher in pH 7.2 (p < 0.0001) and pH 6.1 (p= 0.0137) buffer solution as compared to 600 °C calcined nano-CaPs, except in buffer solution of pH 4.1 (p= 0.3842).

3.4.3 Dissolution kinetic of CaP nanoparticles—The rate of dissolution of nano-CaPs in different pH solution was evaluated by measuring Ca^{2+} ion concentration in supernatant using atomic absorption spectroscopy (AAS). Nano-CaPs found to dissolve at an increasingly faster rate with a decrease in buffer pH from 7.2 to 4. Also at all pH, the rate of dissolution for 800 °C calcined nano-CaPs was always higher ($p < 0.0001$) compared to 600 and 700 °C calcined NPs as evident from Figure 11a, b and c.

4. Discussion

NP12 surfactant stabilized the aqueous core in reverse micelle domain by organizing polar head groups away from non polar cyclohexane in a definite shape. The polar aqueous core contained Ca^{2+} and PO_4^{3-} ions with a Ca:P molar ratio equal to 1.5:1. Addition of NH_4OH in the microemulsion increased OH^- concentration and promoted nucleation of CDHA $[Ca_9(HPO_4)(PO_4)_5(OH)]$ crystal inside polar core of reverse micelle and finally precipitated out in the reaction mixture. The chemical reaction that occurred inside the nanodroplets of water was as follows.

$$9\,Ca(NO_3)_2 + 6\,H_3PO_4 + 18\,NH_4OH = Ca_9(HPO_4)(PO_4)_5(OH) \downarrow + 18\,NH_4NO_3 + 17\,H_2O \tag{1}$$

In this study, the synthesized nano-CaPs showed different crystalline phases with change in calcination temperature as shown in Figure 1 and Figure 2, which is consistent with previous reports.[36] The FTIR spectra in Figure 2 shows characteristic bands of phosphate group at wave numbers 476, 563, 601, 985, 1025, and 1091 cm^{-1} for all the nano-CaPs.[37,38] The bands at 1025 and 1091 cm^{-1} were assigned to the components of triply degenerate ν_3 antisymmetric P–O stretching mode. The non degenerate P–O symmetric stretching mode ν_1 was detected at 985 cm^{-1}. The bands at 601 and 563 cm^{-1} were attributed to components of the triply degenerated ν^4 O–P–O bending mode and the doubly degenerate ν^2 O–P–O bending mode was evident at 476 cm^{-1}. The most noticeable change in the FTIR spectra with increasing calcination temperature was the disappearance of HPO_4^{2-} band at 870 cm^{-1} and hydroxyl band at 3569 cm^{-1} which was also reflected in the phase transformation observed in XRD pattern, as shown in Figure 1.[39] Nano-CaPs calcined at 800 °C showed a broader band at 900–1200 cm^{-1} as compared to powders calcined at lower temperature, which is characteristic to β-TCP phase. The absence of ν_4 PO_4^{3-} band at 620 cm^{-1} confirmed the absence of β–TCP phase in the synthesized powders.[40] The CDHA phase transformed into β-TCP on heating at 800 °C according to following equation.[36]

$$Ca_9(HPO_4)(PO_4)_5(OH) \rightarrow 3\,Ca_3(PO_4)_2 + H_2O \tag{2}$$

Moreover, the absence of OH bending frequency in FTIR spectra of CaP 800 compared to CaP 700 and CaP 600 spectra can be explained due to pure β-TCP phase formation in CaP 800 instead of CDHA as major phase for CaP 700 and CaP 600.

With an increase in calcination temperature, size of nano-CaPs increased as shown in Figure 3, a variation that was not statistically significant. The decrease in particle aspect ratio with a similar increase in calcination temperature, as analyzed from the TEM micrographs in Figure 4, is attributed to the phase transformation of CDHA into β-TCP with loss of one molecule of water along c-axis of CDHA nanocrystal. As depicted in Figure 5, nano-CaPs calcined at 600 °C showed the highest average BET surface area not only because of its smaller particle size, but also due to higher particle aspect ratio. The BET specific average surface area for powders calcined at 600 °C and 800 °C are 73 m^2/g and 57 m^2/g respectively, where the difference is statistically significant.

The interactions between BSA and nano-CaPs were a dynamic process of adsorption and desorption which reached equilibrium within 6h as shown Figure 6. Here BSA loading on nano-CaPs was studied at pH $\geq$ 7.5, because at lower pH the dissolution of nano-CaPs could destroy a stable interface between BSA and nanoparticles. Since pH of BSA - CaP suspension was above the isoelectric points of each of BSA, β-TCP and CDHA, both BSA and nano-CaPs carried negative charges on their surface. The stern layer of anions $[A^-, (H_2PO_4^-, OH^-)]$ attached to Ca^{2+} ions was the source of negative charge on CaP nanoparticle surface. This layer was followed by a diffuse electrical double layer around the surface of nano-CaPs as depicted in Figure 7. BSA interacted with nano-CaPs through electrostatic interaction between COO^- and Ca^{2+}.[41] For successful BSA adsorption on CaP nanoparticle surface, the energy released due to C^{2+}-COO^- interaction should supersede the sum of energy released for Ca^{2+} - A^- attractive interaction and repulsion between BSA molecule and electrical double layer around CaP particle surface. The electrostatic interaction between Ca^{2+} and COO^- was energetically favorable when BSA protein radius (R_{pro}) was greater than the Debye length or thickness of electrical double layer (δ_e) around the particle surface.[42] As pH of the suspension increased from 7.5 to 8.5 to 9, an enhanced charge density on particle surface made Ca^{2+}-A^- interaction increasingly stronger with a subsequent gradual increase in electrical double layer thickness (δ_e) around the CaP nanoparticle surface.[43] This enhanced the electrostatic repulsion force between particle surface and BSA. The increased repulsive interaction coupled with shortening of BSA protein radius (R_{pro}) with increase in pH rendered BSA- nanoparticle interactions increasingly unfavorable.[41,43] Thus the amount of BSA adsorbed onto CaP NP surface was gradually decreased with increase in pH from 7.5 to 9, as shown in Figure 6. Figure 8 shows that the adsorbed amount of BSA increased with increase in surface area of nano-CaPs immersed in BSA solutions. Higher the surface area, higher was the surface charge density of nano-CaPs, resulted in a higher degree of electrostatic interaction between BSA and nano-CaPs.[32]

We have performed the secondary structure analysis of BSA after its adsorption onto CaP nanoparticle surface as shown in Table 1 and Figure 9. The FTIR spectra of BSA adsorbed nano-CaPs in Figure 9 confirmed the presence of BSA in all the nano-CaPs. The spectrum of BSA exhibited an apparent absorption band at 1654 cm^{-1} assigned to amide I CMO stretching mode, 1540 cm^{-1} assigned to amide II N–H bending mode and 1397 cm^{-1} assigned to amide III C–N stretching mode and N–H bending mode.[24] In general α-helix content is a preferred indicator of protein's structural integrity. β-sheet content in protein may alter due to protein–protein interactions leading to the formation of intermolecular β-sheet. Consequently, the β-sheet content of a protein in solid form does not reflect its actual intramolecular structural content. The decrease in α-helix content in CaP-BSA nanoparticles indicates that BSA's secondary structural integrity was somehow distorted on its adsorption to nano-CaP surface. The distortion in secondary structure in BSA is attributed to unidirectional electrostatic interaction between Ca^{2+} and COO^-.[32]

The first layer of BSA was adsorbed onto nanoparticle surface purely by virtue of electrostatic interaction between nano-CaPs and BSA. The adsorption of subsequent layers of BSA was mainly governed by intermolecular hydrophobic interactions as BSA molecules experienced gradually lesser extent of electrostatic interaction with increasing thickness of BSA layers on nanoparticles surface. That is why a number of BSA layers were adsorbed on CaP nanoparticle surface which were not tightly bound.[24] The initial burst release of BSA from particle surface, as shown in Figure 10, was mainly due to desorption of these loosely bound BSA molecules. The release of BSA increases with decrease in pH of the release media in the order of 7.2<6.1<4.1. Always, there exists an adsorption-desorption equilibrium between BSA adsorbed on the surface of nanoparticle and BSA released in the media. At physiological pH, the solubility product of β-TCP ($K_{sp} \approx 2.27 \times 10^{-27}$) is much higher compared to that of CDHA ($K_{sp} \approx 2.35 \times 10^{-49}$). Thus 800 °C calcined nano-CaPs having the highest amount of β-TCP

phase, showed higher rate of dissolution than nano-CaPs calcined at 600 and 700 °C at all pHs studied here. The similar trend in BSA release rate with CaP nanoparticle dissolution rate in Figure 11 revealed the fact that later stage of BSA release was mainly controlled by particle dissolution to release tightly bound BSA molecules. However, for the initial time period, the rate of dissolution of CaP nanoparticles was almost the same for all the CaPs irrespective of the phase composition in CaP nanoparticles. Thus, no difference in the BSA release is observed for the initial time period, irrespective of the calcination temperature. The higher BSA release from 700 °C calcined nano-CaPs as compared to 600 °C calcined nano-CaPs is attributed to the presence of little amount of β-TCP phase in the former.

The dissolution of CDHA and β-TCP nanoparticles can be explained by following equations.

$$Ca_9(HPO_4)(PO_4)_5(OH)+19H^+ \leftrightarrow 9Ca^{2+}+9H_2PO_4^-+H_2O \tag{3}$$

$$Ca_3(PO_4)_2+4H^+ \leftrightarrow 3\,Ca^{2+}+2H_2PO_4^- \tag{4}$$

As the pH of buffer solution decreased, the H^+ concentration in buffer solution increased. The increase in H^+ concentration forced the dissolution equilibrium to be shifted towards right, making dissolution of nano-CaPs faster. At lower pH, CaP nanoparticle dissolution being much higher than that at physiological pH, the BSA release rate was also faster. Thus for relatively faster release of drugs and biomolecules β-TCP nanocarriers should be used, whereas CDHA nanocarrierrs are useful for slower release of carried therapeutics or biologically active molecules. For further precise control over the release of active pharmaceutical ingredients, a mixture of CDHA and β-TCP nanocarriers in different proportion can be used.

5. Conclusions

CaP nanoparticles were synthesized using reverse micelle method. Amount of BSA loading on these nano-CaPs depended on their BET specific average surface area. BSA release kinetics varied depending on phase composition of nano-CaPs and pH of buffer solution in which BSA-nano-CaPs were immersed. The rate of dissolution of β-TCP phase in buffer medium being much higher compared to CDHA phase, 800 °C calcined nano-CaPs showed higher BSA release rate than nano-CaPs calcined at 600 and 700 °C. With decreasing pH of buffer solution, the rate of dissolution of nano-CaPs became increasingly higher, which was reflected in higher rate of BSA release at pH 6 and 4 as compared to pH 7.2. The study showed that protein release rate can be controlled by varying particle size, surface area, and phase composition of CaP nanocarriers.

Acknowledgments

References

1. Garnett MC. Gene-delivery systems using cationic polymers. Critical Reviews in Therapeutic Drug Carrier Systems 2004;16:147–207. [PubMed: 10706442]

2. Heiser, WC. Gene Delivery to Mammalian Cells. New Jersey: Humana Press; 2004. p. 1-35.

3. Jin S, Ye K. Nanoparticle-mediated drug delivery and gene therapy. Biotechnol. Prog 2007;23:32–41. [PubMed: 17269667]

4. Tripathy SK, Black HB, Goldwasser E, Leiden JM. Long-term expression of erythropoietin in the systemic circulation of mice after intramuscular injection of a plasmid DNA vector. Nat Med 1996;93:10876–10880.

5. Chollet P, Favrot MC, Hurbin A, Coll JL. Side-effects of a systemic injection of linear polyethylenimine-DNA complexes. J. Gene Med 2002;4:84–91. [PubMed: 11828391]

6. Zelphati O, Nguyen C, Ferrari M, Felgner J, Tsai Y, Felgner PL. Stable and monodisperse lipoplex formulations for gene delivery. Gene Ther 1998;5:1272–1282. [PubMed: 9930330]

7. Schmidt HT, Gray BL, Wingert PA, Ostafin AE. Assembly of Aqueous-Cored Calcium Phosphate Nanoparticles for Drug Delivery. Chem. Mater 2004;16:4942–4947.

8. Yang J, Lee J, Kang J, Lee K, Suh JS, Yoon HG, Huh YM, Haam S. Hollow Silica Nanocontainers as Drug Delivery Vehicles. Langmuir 2008;24:3417–3422. [PubMed: 18324841]

9. Chen CC, Lin YP, Wang CW, Tzeng HC, Wu CH, Chen YC, Chen CP, Chen LC, Wu YC. DNA-Gold Nanorod Conjugates for Remote Control of Localized Gene Expression by near Infrared Irradiation. J. Am. Chem. Soc 2006;128:3709–3715. [PubMed: 16536544]

10. Salem AK, Searson PC, Leong KW. Multifunctional nanorods for gene delivery. Nature Materials 2003;2:668–673.

11. Lim IIS, Ouyang J, Luo J, Wang L, Zhou S, Zhong CJ. Multifunctional Fullerene-Mediated Assembly of Gold Nanoparticles. Chem. Mater 2005;17:6528–6531.

12. Joshi HM, Bhumkar DR, Joshi K, Pokharkar V, Sastry M. Gold nanoparticles as carriers for efficient transmucosal insulin delivery. Langmuir 2006;22:300–305. [PubMed: 16378435]

13. Krueger A. New Carbon Materials: Biological Applications of Functionalized Nanodiamond Material. Chem. Eur. J 2008;14:1382–1390.

14. Fuertes AB, Matra S, Teresa VS, Pedro T. Synthetic Route to Nanocomposites Made Up of Inorganic Nanoparticles Confined within a Hollow Mesoporous Carbon Shell. Chem. Mater 2007;19:5418–5423.

15. Fuertes AB, Teresa VS, Marta S. Fabrication of Monodisperse Mesoporous Carbon Capsules Decorated with Ferrite Nanoparticles. J. Phys. Chem. C 2008;112:3648–3654.

16. Liu C, Zhang ZJ. Size-Dependent Superparamagnetic Properties of Mn Spinel Ferrite Nanoparticles Synthesized from Reverse Micelles. Chem. Mater 2001;13:2092–2096.

17. Xu PZ, Lu GQ. Layered double hydroxide nanomaterials as potential cellular drug delivery. Pure Appl. Chem 2006;78:1771–1779.

18. Sokolova VV, Radtke I, Heumann R, Epple M. Effective transfection of cells with multi-shell calcium phosphate-DNA nanoparticles. Biomaterials 2006;27:3147–3153. [PubMed: 16469375]

19. Habibovic P, Barrere F, Van Blitterswijk CA, De Groot K, Layrolle P. Biomimetic hydroxyapatite coating on metal implants. J. Am. Ceram. Soc 2002;85:517–522.

20. Gorbunoff MJ. The interaction of proteins with hydroxyapatite. I. Role of protein charge and structure. Anal. Biochem 1984;136:425–432. [PubMed: 6721142]

21. Zambonin G, Camerino C, Greco G, Patella V, Moretti B, Grano M. Hydroxyapatite coated with hepatocyte growth factor (HGF) stimulates human osteoblasts in vitro. J. Bone Joint Surg [Br] 2000;82B:457–460.

22. Okubo Y, Bessho K, Fujimura K, Kusumoto K, Ogawa Y, Iizuka T. Osteogenesis by recombinant human bone morphogenetic protein-2 at skeletal sites. Clin. Orthop 2000;375:295–301. [PubMed: 10853181]

23. Ono I, Ohura T, Murata M, Yamaguchi H, Ohnuma Y, Kuboki Y. A Study on Bone Induction in Hydroxyapatite Combined with Bone Morphogenetic Protein. Plast Reconstr Surg 1992;90:870–876. [PubMed: 1329127]

24. Liu TY, Chen SY, Liu DM, Liou SC. On the study of BSA-loaded calcium-deficient hydroxyapatite nano-carriers for controlled drug delivery. J. Controlled Release 2005;107:112–121.

25. Matsumotoa T, Okazakib M, Inouec M, Yamaguchic S, Kusunosec T, Toyonagaa T, Hamadaa Y, Takahashi J. Hydroxyapatite particles as a controlled release carrier of protein. Biomaterials 2004;25:3807–3812. [PubMed: 15020156]

26. Jung UW, Choi SY, Pang EK, Kim CS, Choi SH, Cho KS. The Effect of Varying the Particle Size of Beta Tricalcium Phosphate Carrier of Recombinant Human Bone Morphogenetic Protein-4 on Bone Formation in Rat Calvarial Defects. J. Periodontol 2006;77:765–772. [PubMed: 16671867]

27. Sun JS, Lin FH, Wang YJ, Huang YC, Chueh SC, Hsu FY. Collagen-Hydroxyapatite/Tricalcium Phosphate Microspheres as a Delivery System for Recombinant Human Transforming Growth Factor-β 1. Artificial Organs 2003;27:605–612. [PubMed: 12823415]

28. Xue W, Bandyopadhyay A, Bose S. Synthesis and characterization of mesoporous calcium silicate for controlled release of bovine serum albumin protein. Acta Biomaterialia. 2009 March; in press doi:10.1016/j.actbio.2009.01.012.

29. Bose S, Saha SK. Synthesis and characterization of hydroxyapatite nanopowders by emulsion technique. Chem. Mat 2003;15:4464–4469.

30. Banerjee A, Bandyopadhyay A, Bose S. Hydroxyapatite nanopowders: Synthesis, densification and cell-materials interaction. Materials Science and Engineering C 2007;27(4):729–735.

31. Dasgupta S, Bose S. Reverse Micelle Templated Synthesis of Tricalcium Phosphate for Bone Graft. Journal of the American Ceramic Society. 2009 accepted to the.

32. Brandes N, Welzel PB, Werner C, Kroh LW. Adsorption-induced conformational changes of proteins onto ceramic particles: Differential scanning calorimetry and FTIR analysis. J. Colloid Interface Sci 2006;299:56–69. [PubMed: 16500671]

33. Baron R, Neff L, Louvard D, Courtoy PJ. Cell-mediated extracellular acidification and bone resorption: evidence for a low pH in resorbing lacunae and localization of a 100-kD lysosomal membrane protein at the osteoclast ruffled border. J. Cell Biol 1985;101:2210–2222. [PubMed: 3905822]

34. Baron R. Molecular mechanisms of bone resorption by the osteoclast. Anat. Rec 1989;224:317–324. [PubMed: 2549811]

35. SAS 9.1, The SAS System for Windows Release 9.1. Cary, NC: SAS Inst.; 2003.

36. Bow JS, Liou SC, Chen SY. Structural characterization of room-temperature synthesized nano-sized β-tricalcium phosphate. Biomaterials 2004;25:3155–3161. [PubMed: 14980410]

37. Legeros, RZ. Calcium Phosphates in Oral Biology and Medicine. Switzerland: Karger; 1991. p. 85-87.

38. Elliott, JC. Studies in Inorganic Chemistry: Structure and chemistry of the apatites and other calcium orthophosphates. Netherlands: Elsevier; 1994. p. 112-115.

39. Siddharthan A, Seshadri SK, Sampath Kumar TS. Rapid Synthesis of Calcium Deficient Hydroxyapatite Nanoparticles by Microwave Irradiation. Trends Biomater. Artif. Organs 2005;18 (2):110–113.

40. Vallet-Regı M, Pena J, Izquierdo-Barba I. Synthesis of β-tricalcium phosphate in layered or powdered forms for biomedical applications. Solid State Ionics 2004;172:445–449.

41. Wassell DTH, Hall RC, Embery G. Adsorption of bovine serum albumin onto hydroxyapatite. Biomaterials 1995;16:697–702. [PubMed: 7578773]

42. Seyrek E, Dubin PL, Tribet C, Gamble AE. Ionic strength dependence of protein-polyelectrolyte interactions. Biomacromolecules 2003;4:273–282. [PubMed: 12625722]

43. Alkan M, Demirbas O, Dogan M, Arslan O. Surface properties of bovine serum albumin – adsorbed oxides: Adsorption, adsorption kinetics and electrokinetic properties. Microporous and Mesoporous Materials 2006;96:331–340.
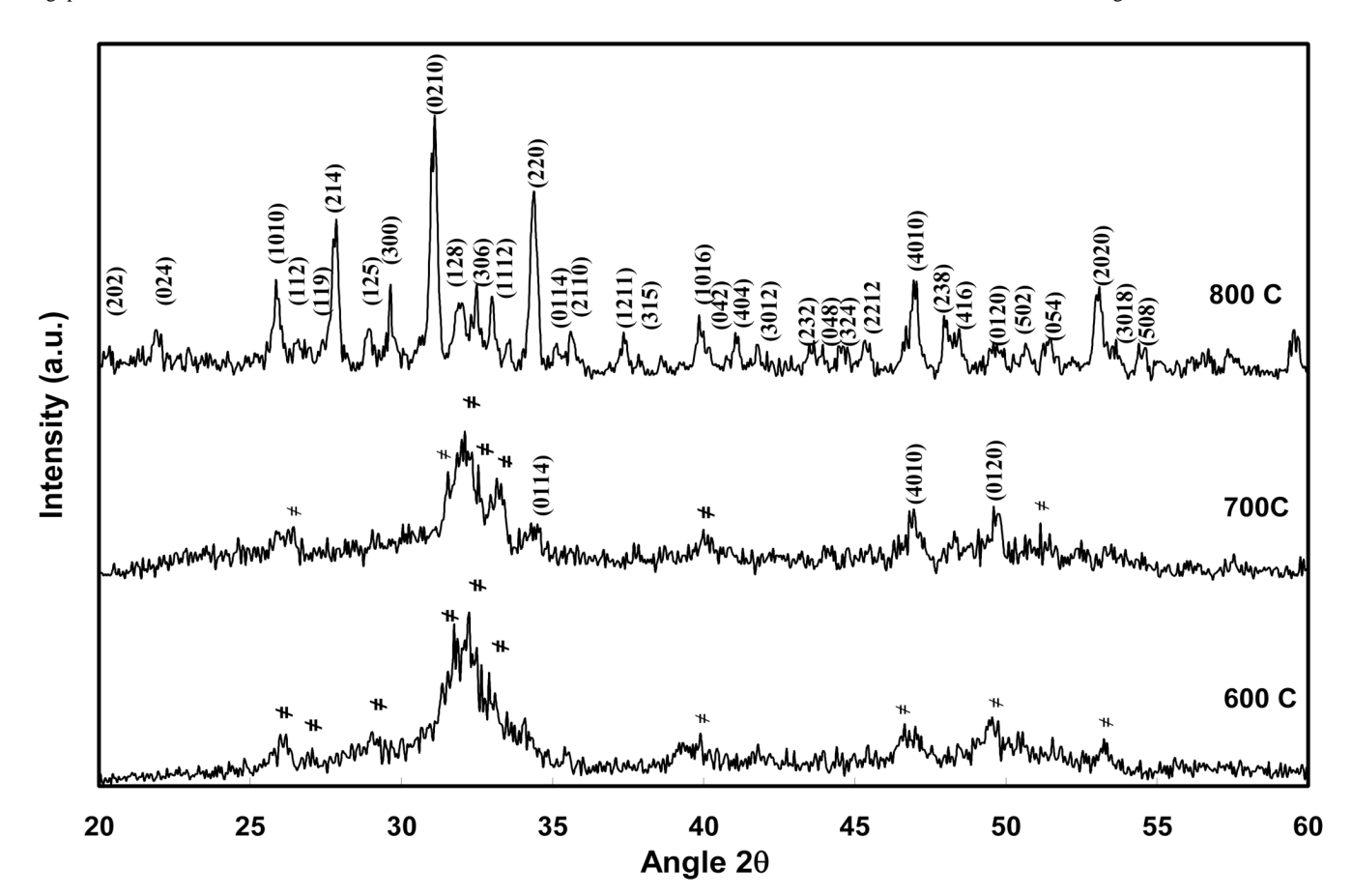
Figure 1.
XRD pattern of synthesized powders calcined at different temperatures.
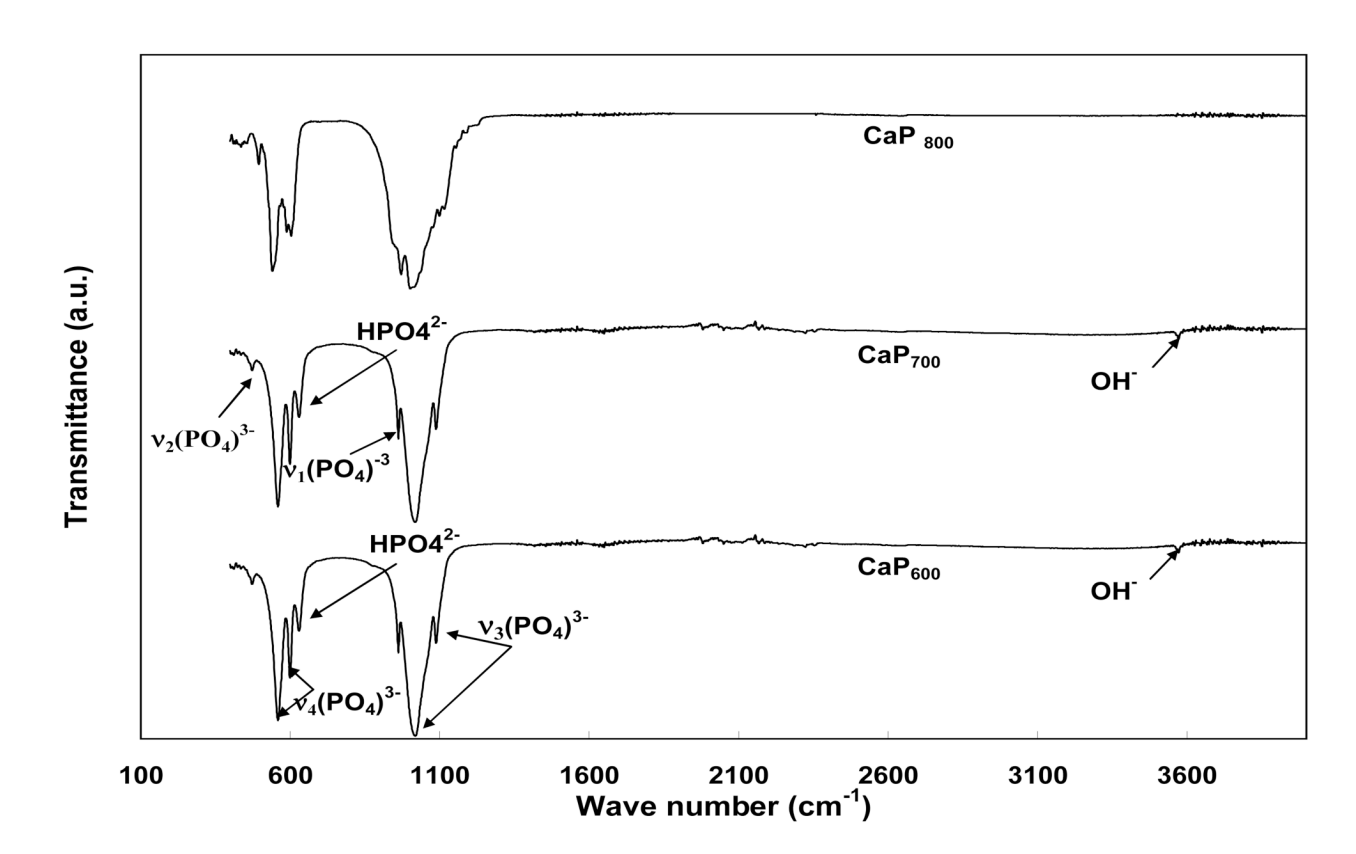'#' shows - CDHA, and all marked (hkl) peaks show β-TCP.

Figure 2.
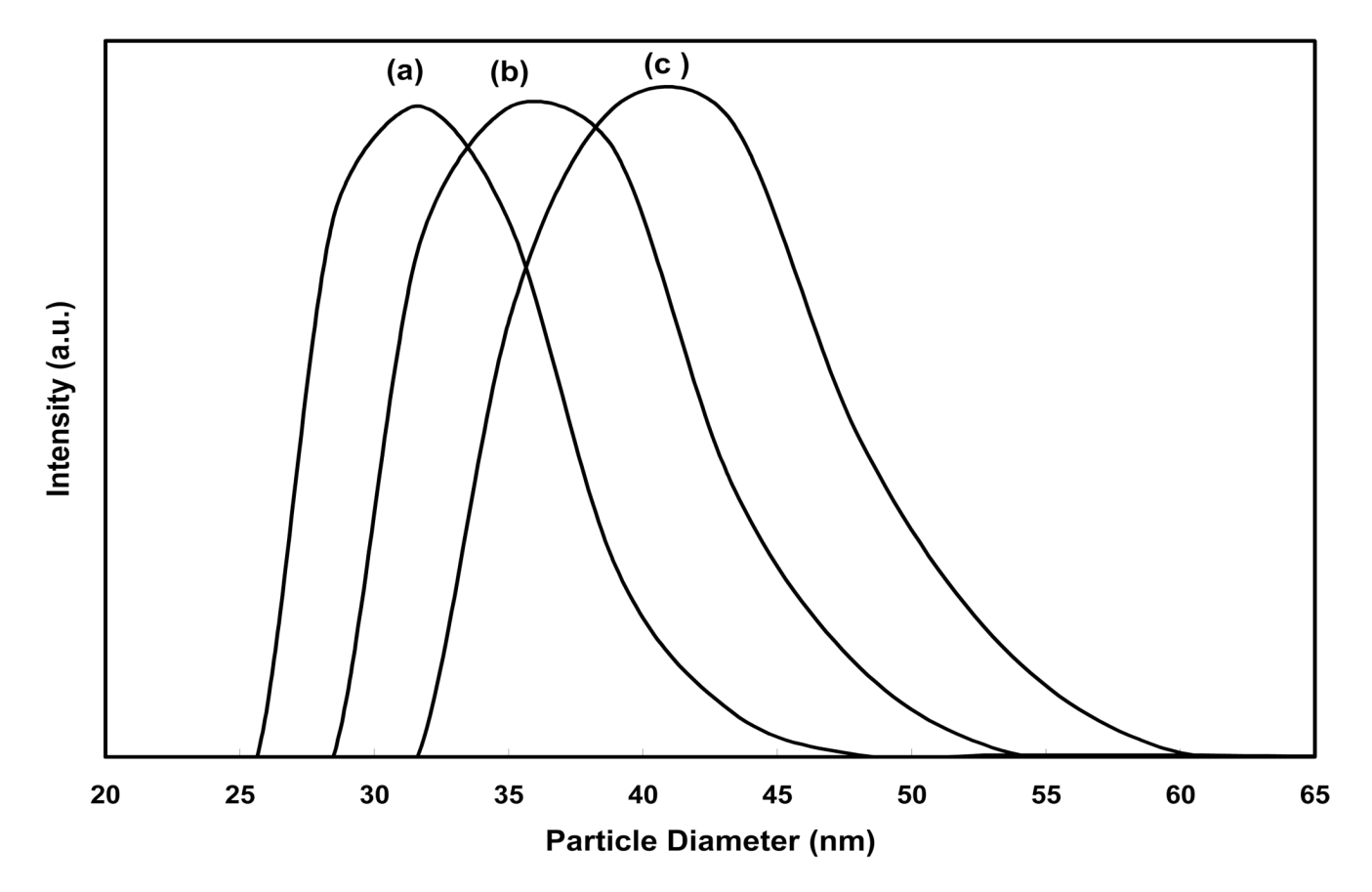FTIR spectra of synthesized CaP nanopowders calcined at different temperature.

Figure 3.
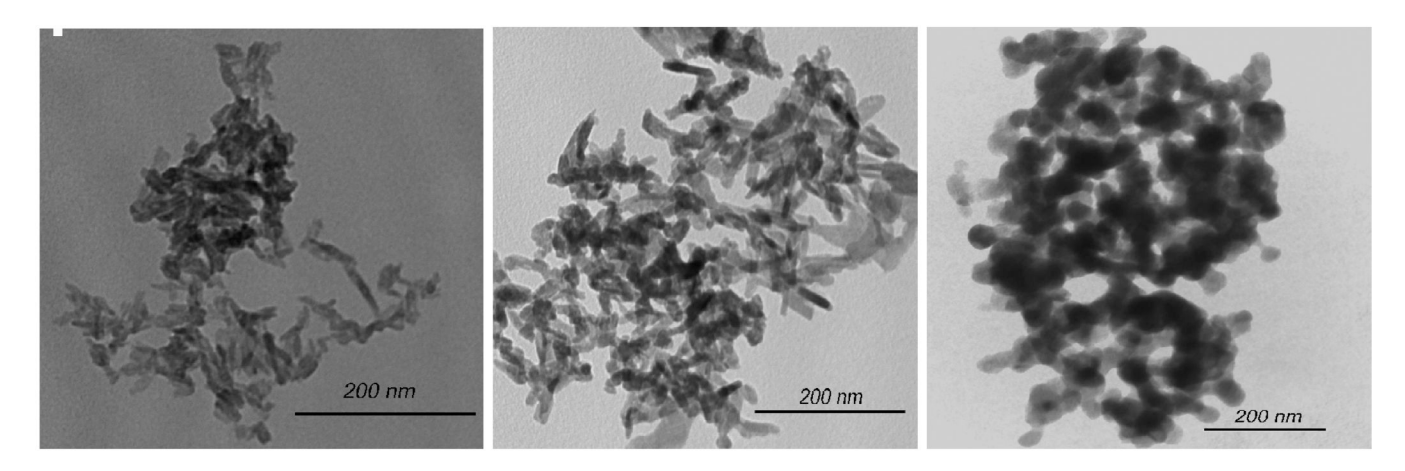Particle size distribution of synthesized nano-CaPs calcined at (a) 600, (b) 700 and (c) 800 °
C.

Figure 4.
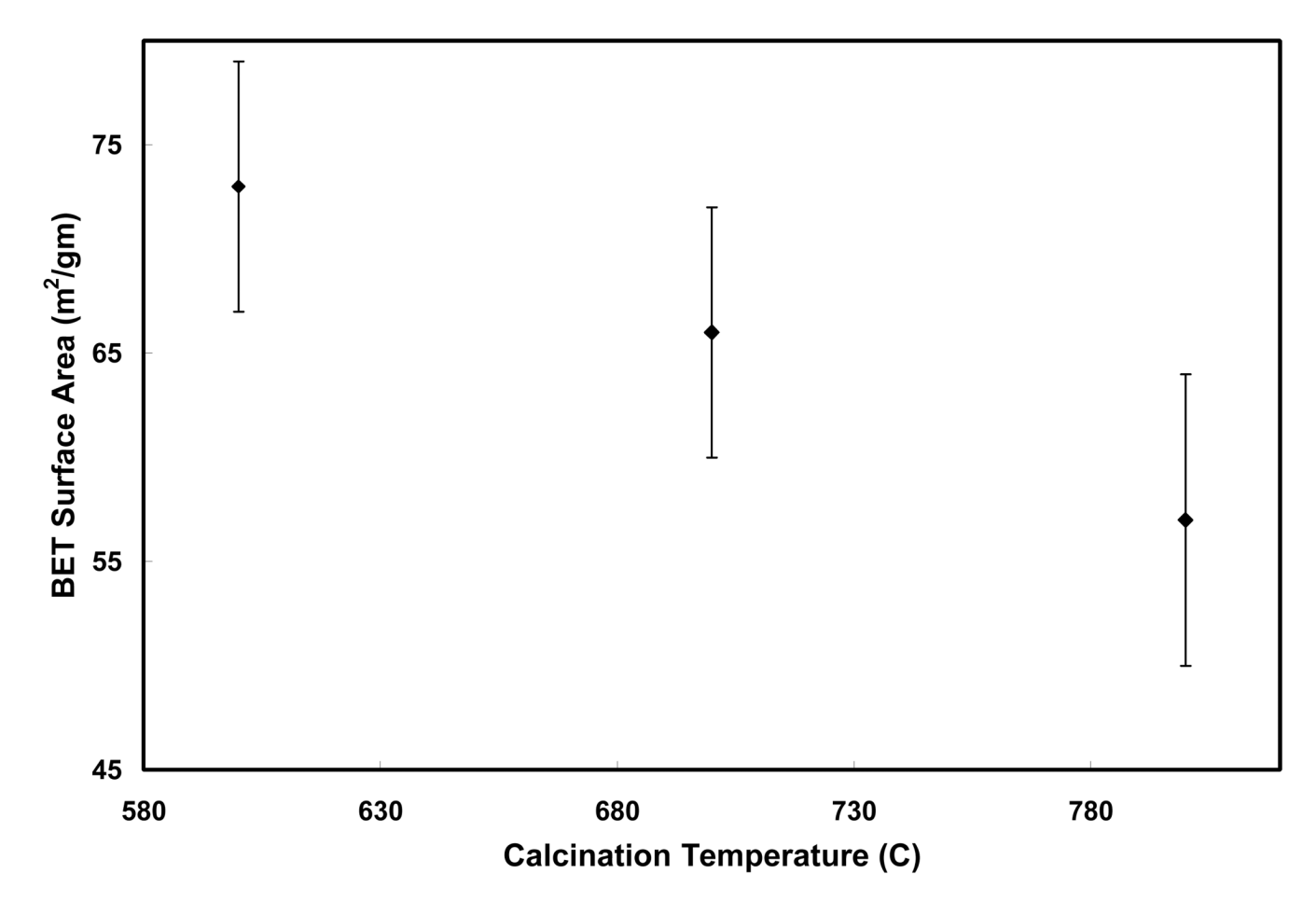TEM micrographs of nano-CaPs calcined at different temperature (a) 600, (b) 700, and (c) 800 °C.

Figure 5.
Variation in BET surface area as a function of calcination temperature
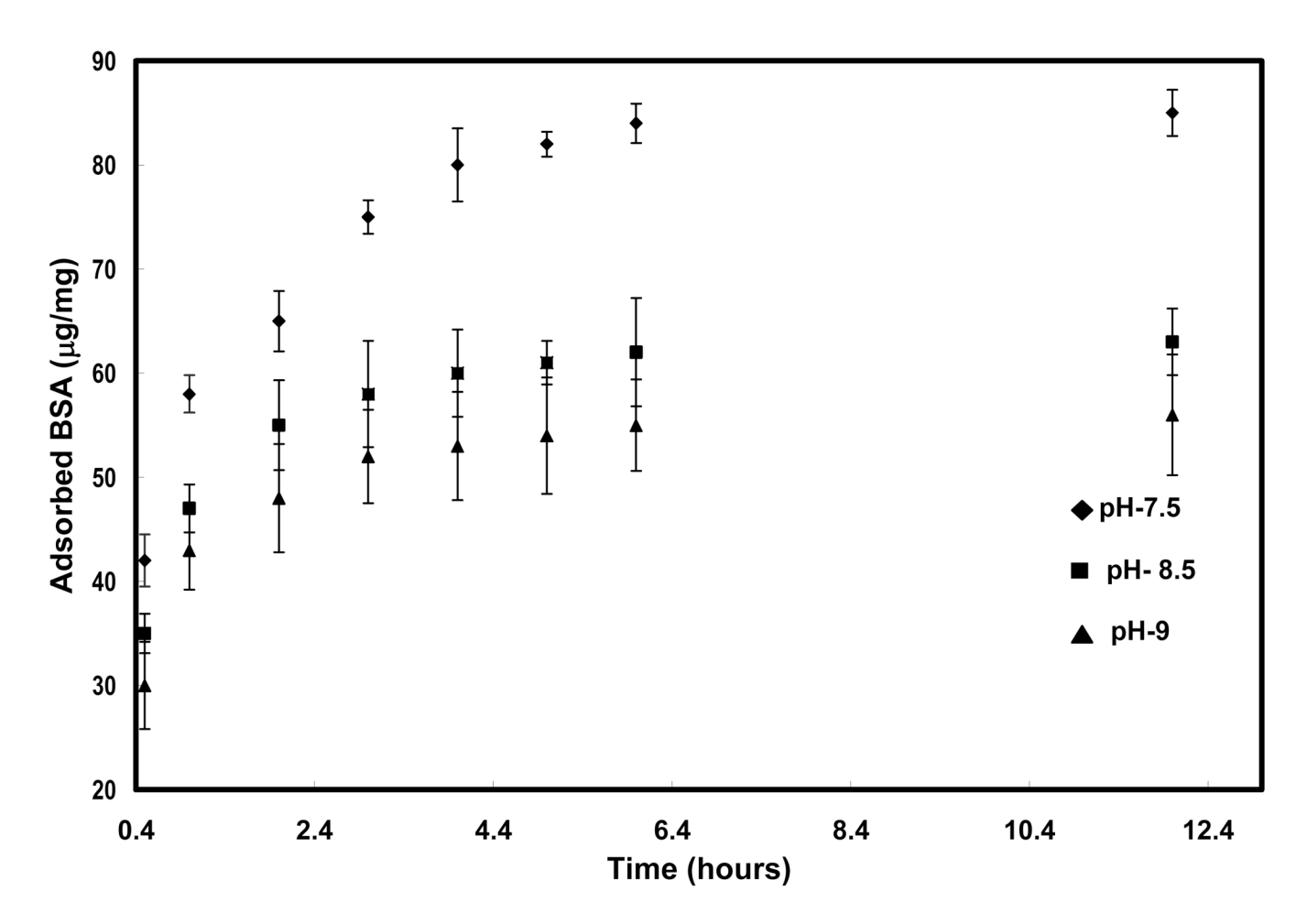
Figure 6.
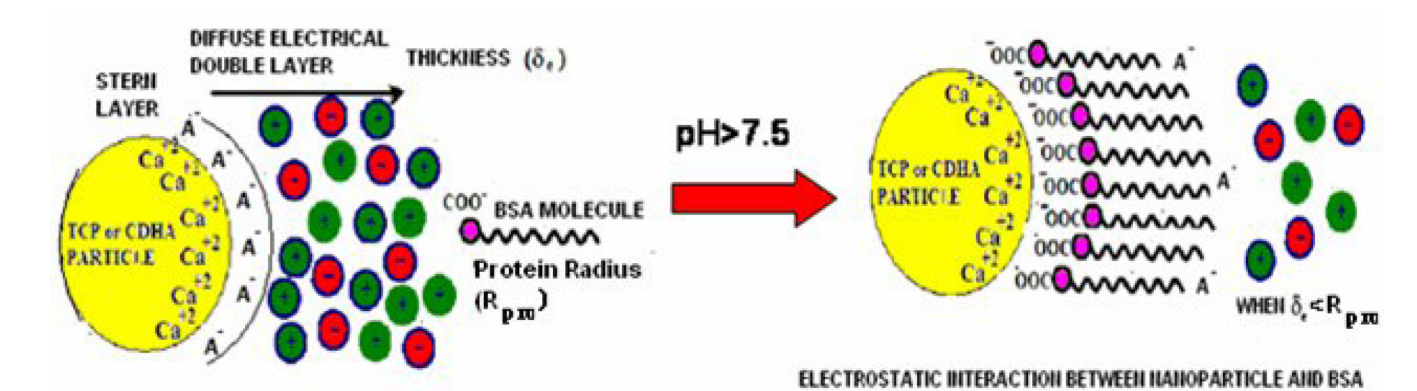Loading of BSA onto CDHA nanoparticle surface at different pH.
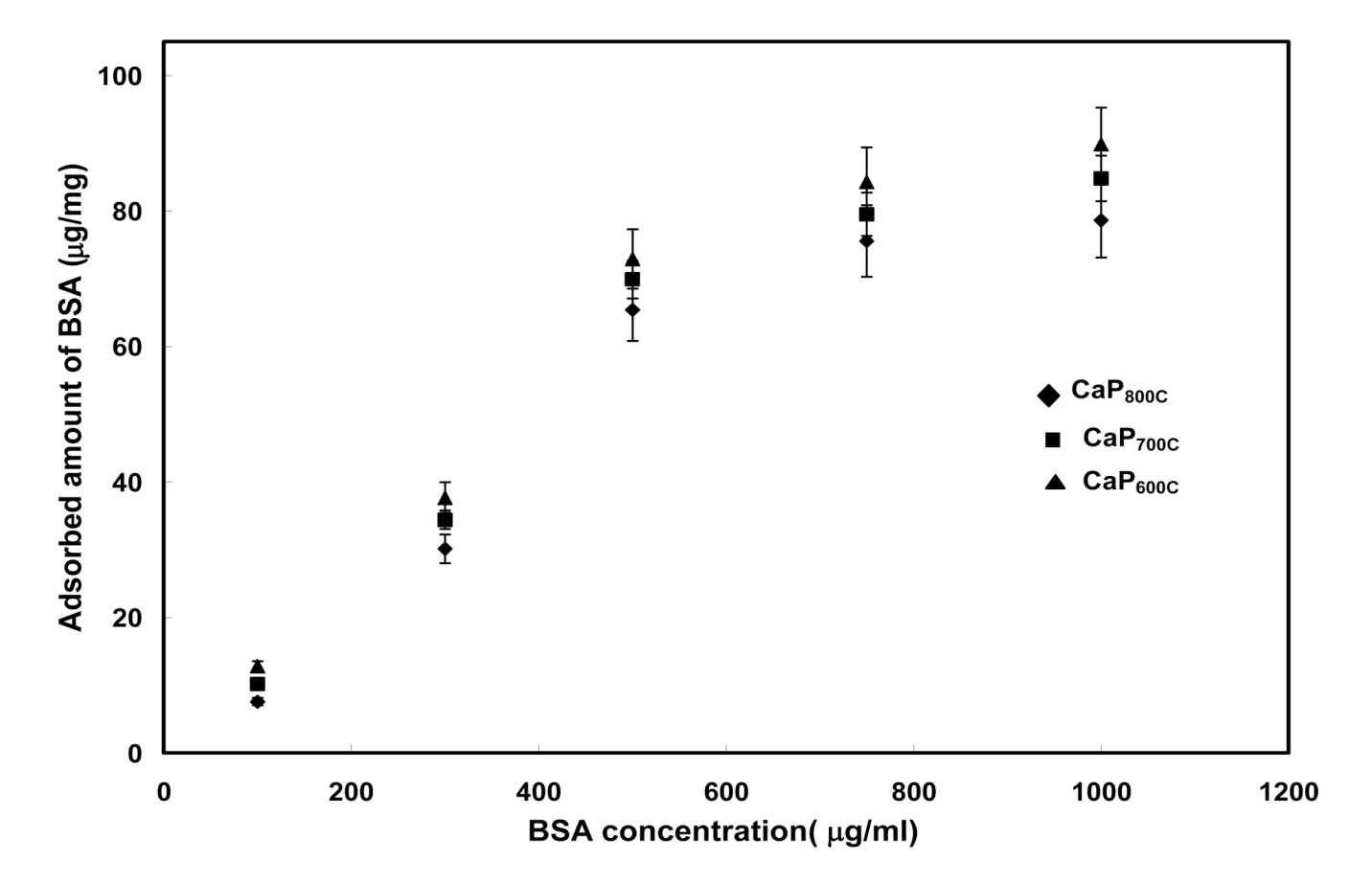
Figure 7.
Schematic representation of BSA – CaP interaction.

Figure 8.
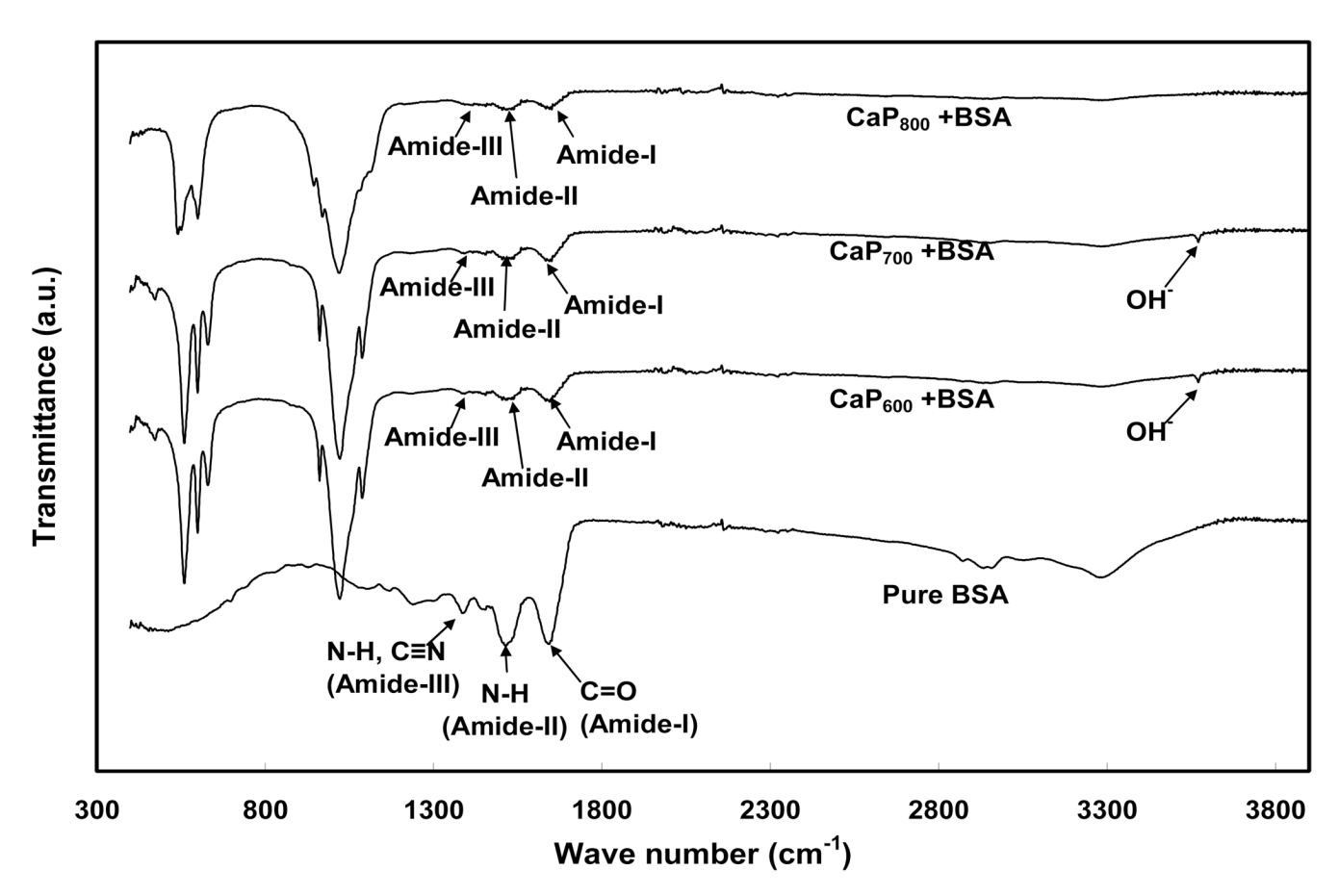Loading of BSA onto nano-CaPs calcined at different temperature.

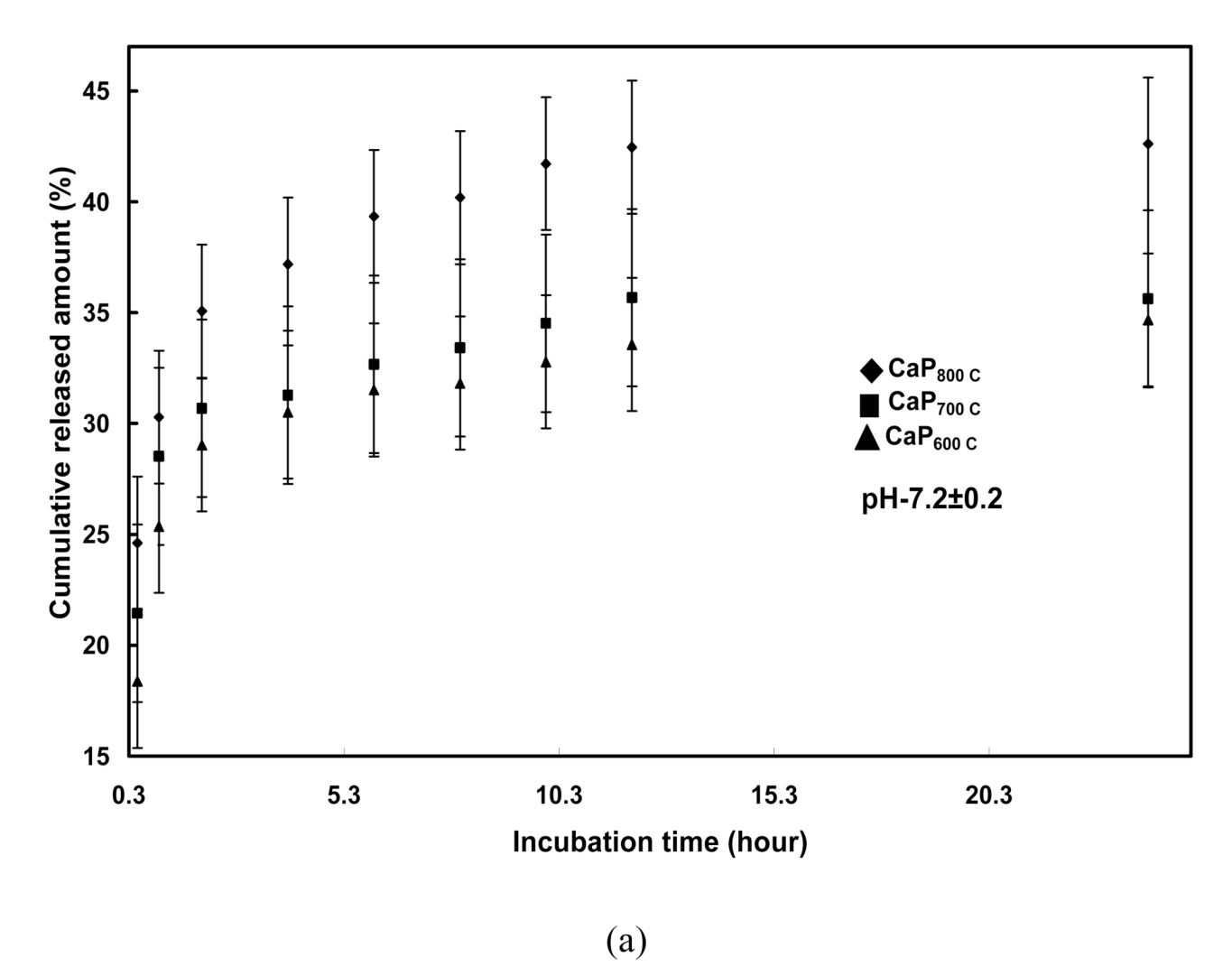**Figure 9.**
FTIR spectroscopy of pure BSA and BSA adsorbed CaP nanopowders.
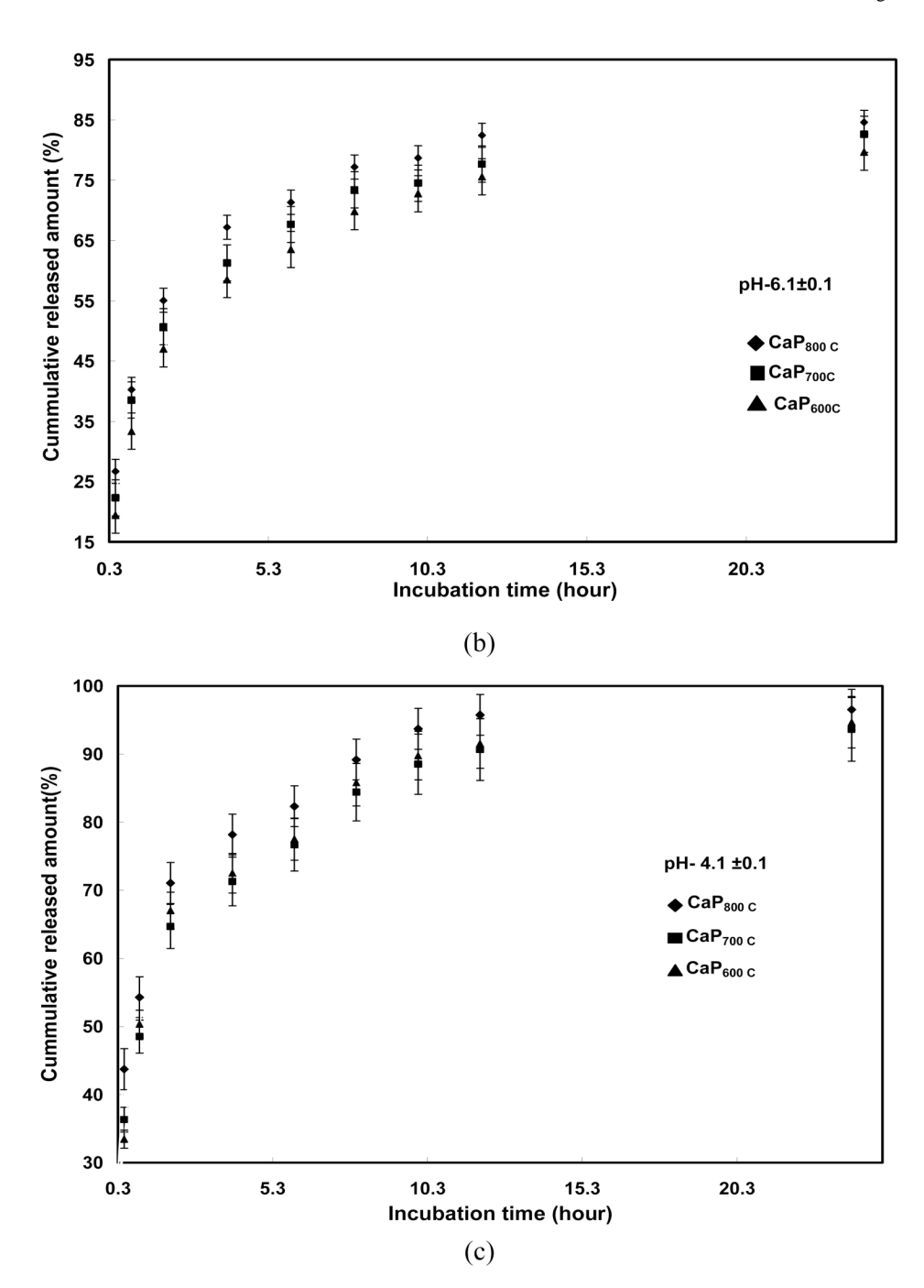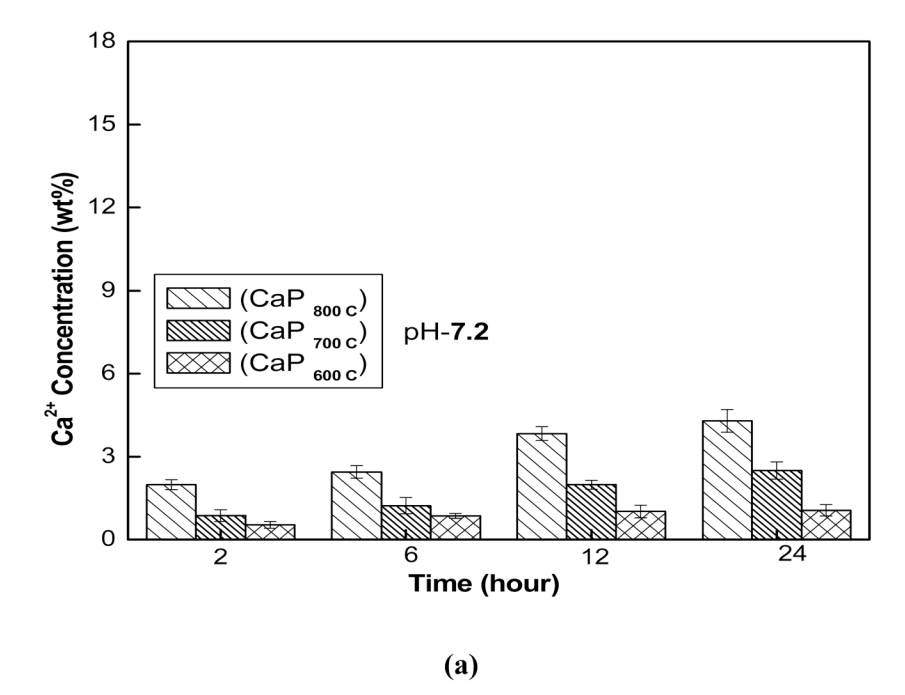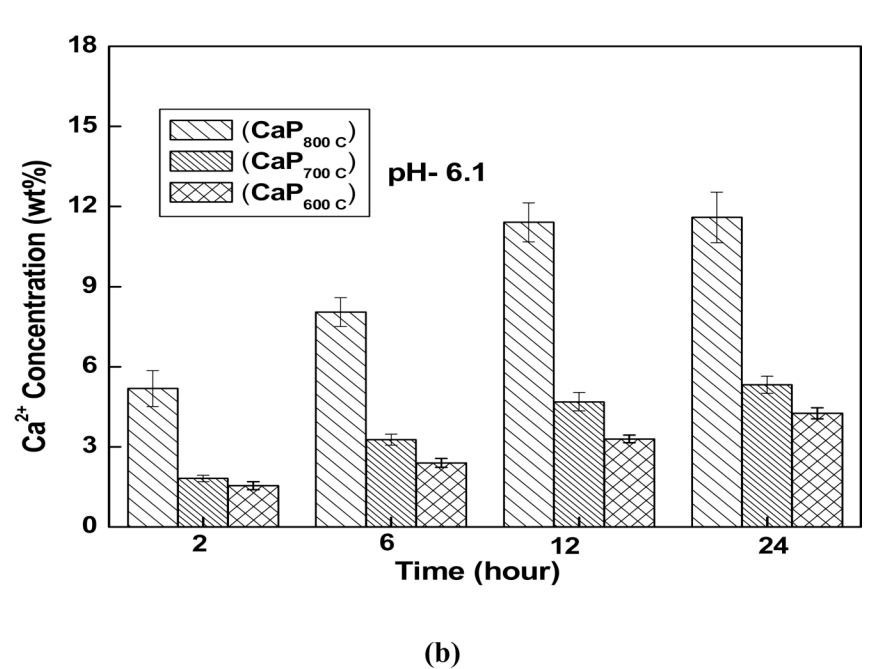
(a)

(b)

(c)

Figure 10.
BSA release rate from nano-CaPs at different pH (a) 7.2, (b) 6.1, and (c) 4.1 Tukey's pairwise multiple comparison test. (a) at pH-7.2; $p < 0.0001$ for CaP_{800} Vs CaP_{700}, $p < 0.0001$ for CaP_{800} Vs CaP_{600}, $p < 0.0001$ for CaP_{700} Vs CaP_{600}; (b) at pH-6.1; $p < 0.0001$ for CaP_{800} Vs CaP_{700}, $p < 0.0001$ for CaP_{800} Vs CaP_{600}, $p = 0.0137$ for CaP_{700} Vs CaP_{600}; (c) at pH-4.1; $p < 0.0001$ for CaP_{800} Vs CaP_{700}, $p = 0.0007$ for CaP_{800} Vs CaP_{600}, $p = 0.3842$ for CaP_{700} Vs CaP_{600}
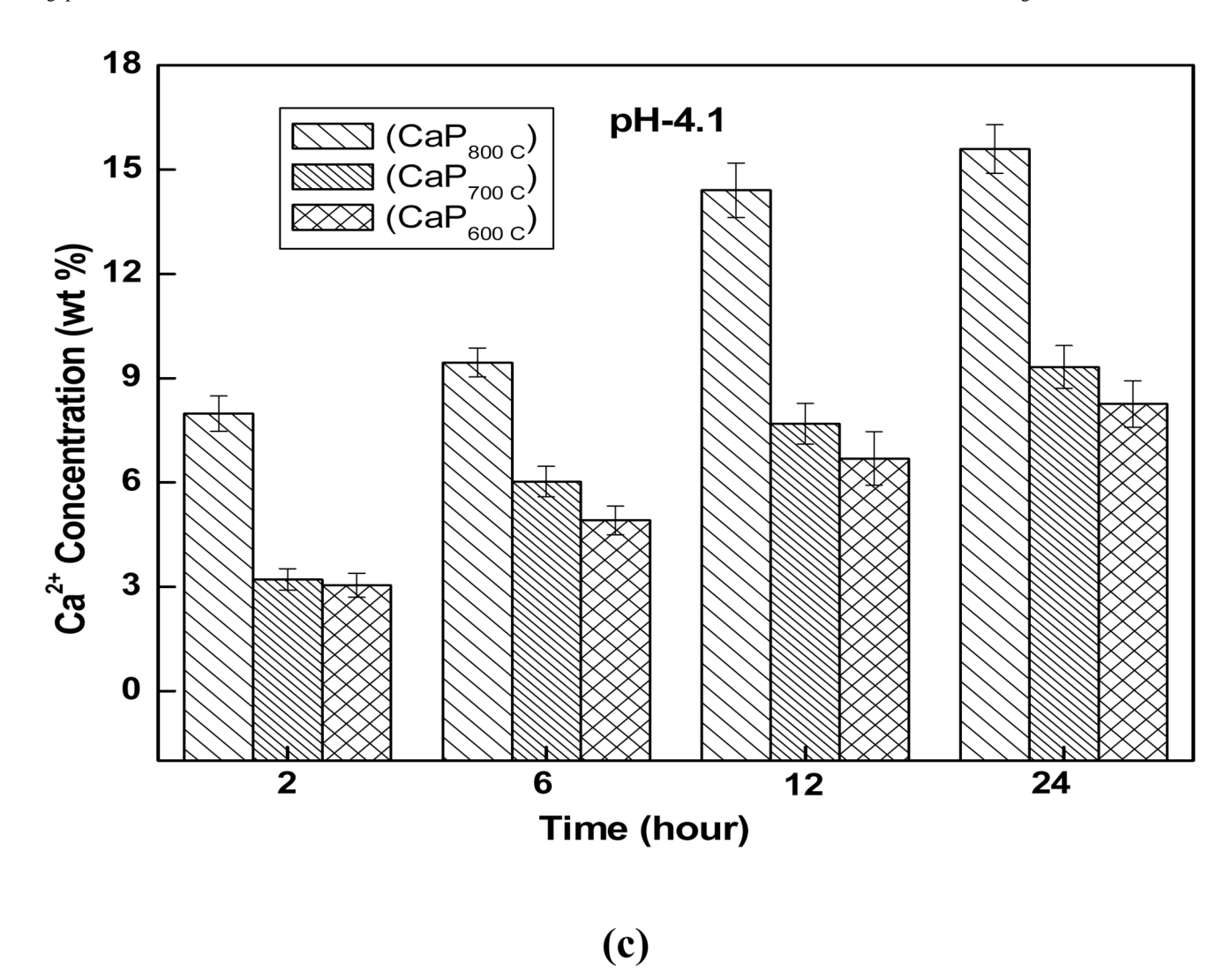
(a)

(b)

(c)

Figure 11.
Dissolution kinetics of nano-CaPs at three different pH (a) 7.2 (b) 6.1, and (c) 4.1. Tukey's pairwise multiple comparison test. (a) at pH-7.2; $p < 0.0001$ for CaP_{800} Vs CaP_{700}, $p < 0.0001$ for CaP_{800} Vs CaP_{600}, $p = 0.012$ for CaP_{700} Vs CaP_{600}; (b) at pH-6.1; $p < 0.0001$ for CaP_{800} Vs CaP_{700}, $p < 0.0001$ for CaP_{800} Vs CaP_{600}, $p < 0.0481$ for CaP_{700} Vs CaP_{600}; (c) at pH- 4.1; $p < 0.0001$ for CaP_{800} Vs CaP_{700}, $p < 0.0001$ for CaP_{800} Vs CaP_{600}, $p < 0.452$ for CaP_{700} Vs CaP_{600}.

Table 1

Infrared band positions of BSA and band assignments

Band position (cm^{-1})	Secondary structure assignment	Area			
		Pure BSA	CaP$_{600}$+ BSA	CaP$_{700}$+ BSA	CaP$_{800}$+ BSA
1616±3	Self association	5±1	8±2	7±1	4±1
1628±3	β-sheet	10±2	14±1	13±2	10±2
1638±3	β-sheet	16±2	19±2	16±1	16±2
1648±3	unordered	17±1	19±1	18±1	19±1
1658±3	α-helix	24±1	18±2	16±2	19±1
1665±3	α-helix	14±1	12±2	15±1	15±1
1671±3	β-turns	10±3	7±2	10±1	10±2
1685±2	β-turns	4±2	3±2	6±1	7±1